Catalysis and Kinetics

Impact of morphological effects on the activity and stability of tungsten carbide catalysts for dry methane reforming

William Pratt Mounfield, Aadesh X. Harale, and Yuriy Roman-Leshkov

Energy Fuels, **Just Accepted Manuscript** • DOI: 10.1021/acs.energyfuels.9b01043 • Publication Date (Web): 15 May 2019

Impact of morphological effects on the activity and stability of tungsten carbide catalysts for dry methane reforming

*William P. Mounfield, III[a], Aadesh Harale[b], and Yuriy Román-Leshkov[a]**

a. Department of Chemical Engineering, Massachusetts Institute of Technology, Cambridge, Massachusetts 02139, USA b. Research & Development Center, Saudi Aramco, Dhahran, KSA 31311

Corresponding Author

*Email: yroman@mit.edu Phone: 617.253.7090 Fax: 617.253.7090 Website: http://romangroup.mit.edu

KEYWORDS

Transition metal carbide; tungsten carbide; carbide; dry methane reforming

ABSTRACT

Fundamental understanding of the effects of phase and exposed facets of transition metal carbide (TMC) catalysts on reactivity is a route to preparing more active and stable materials for targeted applications. In this work, two geometries of tungsten carbide nanomaterials, nanorods and nanoparticles, with differing exposed facets were synthesized to investigate the impact of morphological effects on catalytic performance for the dry methane reforming (DMR) reaction. β-W_2C nanoparticles maintained high activity and exhibited less coke formation for more than 40000 turnovers while α-WC nanorods began to deactivate after only 8000 turnovers. The difference in reactivity is attributed to the promotion of coke formation by the exposed facets of the nanorods while the diverse facets of the nanoparticles inhibit coke formation and promote the DMR reaction. The synthesis of a variety of TMC morphologies provides an avenue for future study and design of viable catalysts for a wide range of applications.

1. INTRODUCTION

With growing concerns over increasing greenhouse gas emissions, there exists a critical challenge to develop technologies and materials to utilize carbon dioxide (CO_2) as a feedstock.[1-2] Dry methane reforming (DMR) is a promising alternative to steam methane reforming for the generation of synthesis gas because CO_2 is used as an oxidant instead of steam, thereby opening a pathway for the utilization of CO_2 as a feedstock for the production of synthetic fuels. DMR is a highly endothermic reaction (ΔH_{298K} = +247.3 kJ/mol) that generates a product mixture with a H_2/CO ratio near unity, which is ideal for iron ore reduction, acetic acid production and can be used to increase selectivity in the Fischer Tropsch process toward the higher hydrocarbons[3] integral to aviation and ground transportation fuels. Although DMR requires a high thermal input to reach appreciable conversions, it has become of increasing commercial interest due to the activities in support of climate concerns.[4] The chemistry of reforming with CO_2 has been studied for decades, yet no robust catalyst exists to perform this reaction on an industrial scale. A main disadvantage of the high temperatures required for the process is the high thermodynamic potential to form coke, resulting in rapid catalyst deactivation. Carbon can be deposited in different forms on the catalyst, either encapsulating the supported metallic nanoparticles, or diffusing into crystal lattice and forming filamentous carbon whiskers that disintegrate the catalyst into finer particles, drastically increasing the pressure drop along the reformer.[5-7] Furthermore, high temperatures often result in sintering and agglomeration of metal particles reducing active surface area.[8] Research efforts on nickel-alumina catalysts have focused on improving the coke and sinter resistance by minimizing particle size and adding small amounts of noble metals (NMs).[9] However, due to the high costs associated with noble metals, more recent efforts have turned the focus to earth-abundant systems such as transition metal carbides (TMCs).[10-17]

TMCs, such as molybdenum carbide and tungsten carbide, have shown promise for many energy applications, including hydrogen evolution, oxygen reduction, isomerization and water-gas shift reactions.[18-26] Many of these studies have evaluated TMCs for replacing or lowering the loading of NMs in catalyst formulations as

originally detailed by Levy and Boudart.[27-29] Advances in synthetic methods have focused on modifying their properties through the synthesis of varying morphologies, including nanoparticles, nanorods, and nanosheets.[8, 30-31] An important, but often overlooked byproduct of these efforts, is the exposure of facets that possess vastly different reactivity. While facet dependent reactivity trends have been studied in depth for thin oxide and metal films,[32-35] few of these studies for TMCs exist computationally,[19, 36] with even fewer experimental studies due to synthetic limitations. A targeted synthesis approach with facet control would allow direct analysis of structure reactivity relationships for TMCs.

Several studies have investigated TMCs for DMR over a wide range of reaction conditions.[10-12, 37-41] Green et al. demonstrated the activity and inherent resistance to macroscopic carbon formation of bulk molybdenum and tungsten carbides.[38] The authors suggested similarities to noble metals as the reason for the observed activity.[29, 42-43] Green et al. expanded the investigation to include other transition metal carbides for DMR, discovering molybdenum and tungsten are the most resistant to deactivation through oxidative pathways.[11] Furthermore, the authors offered some insight into the disparate catalytic behavior between the TMCs by calculating the temperature at which recarburization becomes favorable for vanadium, tungsten and molybdenum carbide. They found this it to be similar across all transition metals; yet found that vanadium carbide did not possess stability similar to the group VI carbides. From this observation, the authors suggested the carbide structure plays an important role in the kinetics of the oxidation/recarburization reaction due to a difference in exposed facets, as vanadium carbide is present in the fcc phase while both tungsten and molybdenum carbide are hexagonal. A similar hypothesis was reached by Thompson et al. in the study of transition metal nitrides (TMNs) and carbides for n-butane hydrogenolysis. TMNs and TMCs with the same metal atom and same crystal phase exhibited similar reactivity regardless of the heteroatom, while those with different structure had markedly different activity, indicating the importance of lattice structure on the reactivity of the catalyst. Furthermore, in a comparison across the several phases of tungsten carbide, hexagonal β-W_2C was the most active phase being slightly more active than hexagonal α-WC, and more than twice as active as fcc WC_{1-x}.[44] These studies also highlight the lack of understanding of the underlying effects of crystal phase, exposed facets, and morphology on activity within TMCs.

Understanding the effects of morphology and facet size on reactivity and stability by way of rational nanostructuring is necessary to develop carbide-based DMR catalysts with improved sinter resistance and enhanced activity.[8, 45] Overall, however, there is a paucity of studies relating the influence of crystallographic facets and morphology on activity and stability of TMCs during DMR. Yu et al. investigated the synthesis of WC nanoparticles in the range of 5-10 nm from tungsten-promoted biochar and subsequent use of the catalysts for DMR.[45] The authors found a uniform particle distribution with little coke formation after 500 h on stream suggesting the small particle size contributed directly to the stability of the catalyst. Wang et al. studied the use of tungsten and molybdenum carbide based catalysts to improve the sinter resistance of nickel-modified catalysts.[8] Ni-WC was found to exhibit better stability than Ni-Mo_2C, which was attributed to the sinter resistance of WC - observed through a similar crystallite size before and after reaction for the tungsten carbide particles. In addition, Ni-WC also proved resistant to oxidation during reaction as little change was observed in the XPS spectra for fresh and used samples while the molybdenum catalyst exhibited a significant decrease in the Mo^{2+} species indicative of oxidation of Mo_2C.

In this work, β-W_2C nanoparticles and α-WC nanorods were synthesized and studied as catalysts for DMR to elucidate the effects of morphology and aspect ratio on activity and stability. Reactions were carried out in packed bed reactors under DMR conditions at 1173 K and 1 atm. Material and textural properties were evaluated using N_2 physisorption at 77 K, high resolution transmission electron microscopy (HRTEM), and powder X-ray diffraction (PXRD) before and after reaction. W_xC was chosen as a representative carbide system not only because it has displayed promising activity and stability for DMR,[8, 11, 45-46] but also because various morphologies of tungsten oxide have been synthesized for use as precursors for the preparation of diverse nanostructured W_xC materials.[47-48] γ-alumina was chosen as the support for the tungsten nanomaterials as it has shown the best stability with Mo_2C over several other oxide supports.[37] Furthermore, γ-Al_2O_3 has also been shown to provide high activity and high stability for Rh-based DMR catalysts.[49-51] Overall, β-W_2C nanoparticles exhibited higher activity and improved coke and sinter resistance than α-WC nanorods, suggesting the disordered phase is more favorable for DMR reactions and may facilitate an oxidation/recarburization reaction pathway that contributes to a more stable catalyst.

2. EXPERIMENTAL

Synthesis of WO_x nanorods. WO_x nanorods were synthesized following the procedure detailed in previous work with some modifications.[48] In a typical synthesis, ammonium metatungstate hydrate (0.1 mmol) was added to 20 mL of oleylamine in a 100 mL round bottom flask and slowly heated to 523 K at a rate of 2 K/min. The suspension was allowed to soak at 523 K for 2 h and cooled to room temperature. After cooling, 80 mL of acetone was added, creating a biphasic solution with dissolved oleylamine in acetone and dispersed nanorods. The resulting blue solution was centrifuged at 5000 rpm for 30 min and the supernatant was removed to yield blue nanoparticles that

could be collected by drying in air at room temperature. The dry blue powder was weighed and dispersed in toluene.

Synthesis of WO_x nanoparticles. WO_x nanoparticles were synthesized following the procedure detailed in previous work with some modifications.[48] In a typical synthesis, ammonium metatungstate hydrate (0.1 mmol) and trimethylamine N-oxide (TANO) (5 mmol) were added to 20 mL of oleylamine in a 100 mL round bottom flask and slowly heated to 523 K at a rate of 2 K/min. The suspension was allowed to soak at 523 K for 2 h and cooled to room temperature. After cooling, 80 mL of acetone was added, creating a biphasic solution with dissolved oleylamine in acetone and dispersed nanoparticles. The resulting yellow solution was centrifuged at 5000 rpm for 30 min and the supernatant was removed yielding nanoparticles that could be collected by drying in air at room temperature. The dry powder was weighed and dispersed in toluene.

Synthesis of W_xC nanorods and nanoparticles. WO_x nanomaterials dispersed in toluene were supported on γ-Al_2O_3 (250-300 nm) through an incipient wetness impregnation (IWI). In a typical synthesis, 5 mL of the suspension of WO_x nanomaterials was added to 1 g of γ-Al_2O_3 to reach a nominal weight loading of 10 wt.% W in a 20 mL scintillation vial. The solution was stirred manually with a spatula to ensure dispersion of the nanomaterials on the support. The solvent was then evaporated in a vacuum oven to yield a dry powder. The dry powder was pelletized and sieved between 150-200 μm. Synthesis of the carbide phase was performed through in situ carburization in a quartz reactor tube. The supported catalysts were subjected to a 2 K/min temperature ramp to 1173 K under a 40 mL/min CH_4:H_2 flow with a 1:4 ratio. The temperature soak was maintained for 1 h followed by a 30 min hydrogen scavenging step under H_2 flow at 32 mL/min, after which the gas flow was switched to the reactant mixture.

Catalytic activity and stability experiments. Activity and stability measurements were performed in a gas-phase packed-bed down-flow reactor. The reactor consisted of a quartz tube (6.35 mm OD, 4 mm ID) mounted in a single-zone furnace (Applied Test Systems, Series 3210, 850 W and 115 V). The temperature was controlled by a temperature controller (Digi-Sense, model 68900-10) connected to a K-type thermocouple (Omega, model TJ36-CAXL-116u) mounted downstream in direct contact with the catalyst bed. Each catalyst was pelletized to 150-200 μm and packed between two 5 mm layers of quartz wool in the middle of the furnace. The total bed volume was ~2 cm^3. Prior to reaction, each catalyst was carburized as detailed in the previous section. After carburization, the carburization flow was switched directly to the reaction mixture of 1:1 CH_4:CO_2 with a total flow rate of 30 mL/min, while maintaining a reaction temperature of 1173 K. The reactor outlet concentrations were analyzed and quantified via an online gas chromatograph (GC) equipped with a thermal conductivity detector (TCD) for identification and quantification (Agilent Technologies, model 6890) The GC was fitted with a Carboxen 1006 PLOT column (Agilent, 30 m × 0.32 mm × 10 μm). The following GC parameters were used for analysis: detector temperature of 463 K, injector temperature of 373 K, and split ratio of 1:1. An isothermal oven temperature of 308 K was used.

The following equations were used to quantify experimental data:

$$\text{conversion (\%)} = \frac{\text{mol reactant consumed}}{\text{mol reactant fed}} \times 100 \quad (1)$$

$$\text{yield (\%)} = \frac{\text{mol product}}{\text{mol reactant fed}} \times 100 \quad (2)$$

$$\text{selectivity (\%)} = \frac{\text{yield}}{\text{conversion}} \times 100 \quad (3)$$

Powder X-ray diffraction. Powder X-ray diffraction patterns were recorded on an Bruker Advance II diffractometer equipped with θ/2θ Bragg-Brentano geometry and Ni-filtered Cu Kα radiation (λ = 1.5418 Å) radiation at room temperature. The tube voltage and current were 40 kV and 40 mA, respectively.

N_2 physisorption. Nitrogen physisorption isotherms were measured at 77 K for samples activated at 623 K for 1 using the Quadrasorb EVO system from Quantachrome instruments. Nitrogen adsorption analysis was performed on all resulting products, and surface areas for the oxide and carbide materials were determined by applying Brunauer-Emmett-Teller (BET) theory over a range of data points derived for oxide materials.[52]

Transmission Electron Microscopy. Transmission Electron Microscopy (TEM) was performed on a JEOL 2010F equipped with a field emission gun (FEG) operating at 200 kV. All examined samples were sonicated for 10 s in toluene and then dispersed on carbon grids (Cu-300) from Sigma Aldrich. Several images were collected for each sample with varying levels of magnification.

3. RESULTS AND DISCUSSION

3.1 Characterization of pristine materials

The phase and morphology of WO_x on γ-Al_2O_3 was investigated with powder X-ray diffraction (PXRD) and transmission electron microscopy (TEM) after synthesis and preparation of each composite. Figure 1 shows the as-prepared diffraction patterns of the supported tungsten oxide nanorods (WO_x-NR), supported tungsten oxide nanoparticles (WO_x-NP), as-received γ-Al_2O_3, and α-Al_2O_3. All samples showed diffraction peaks associated only with the γ-Al_2O_3 support before carburization, with tungsten oxide nanomaterials having no observable reflections at the chosen nominal loading of 10 wt.%. TEM

images of the unsupported WO_x nanomaterials are shown in Figure 2a,b. WO_x-NR features a nanorod morphology with a particle size distribution of 3.96±0.86 nm x 16.49±2.93 nm. The rods exhibit preferential growth along the [010] direction with the [100] family of planes being the primary exposed facet on the sides of the rods, in agreement with the previous report by Wong et al.[48] Figure 2b shows unsupported WO_X nanoparticles with a particle size distribution of 5.96±1.43 nm. The small size of the nanoparticles allows for a variety of facets to be exposed, in contrast with the nanorods where only two different facets are exposed, one along the edges of the rod and one on the basal plane along the direction of growth of the rod.

Table S1 shows the loading on a per mass basis as determined by energy dispersive X-ray spectroscopy (EDX) analysis and the BET surface area for each supported catalyst. The loading on a W wt.% basis is consistent across each sample, and within error of the initial nominal loading, allowing for a direct comparison between samples on a W wt.% basis. The unreacted supported catalysts exhibit high surface area similar to the surface area of the bare γ-Al_2O_3 support. Due to the low nominal loading of each catalyst and the inherent error in N_2 physisorption measurements it was difficult to determine an accurate surface area of either the nanorods or nanoparticles before reaction; instead, the surface area before reaction was used as one measure of coke deposition for the catalysts after reaction. To approximate the active area and thereby the number of active sites for each catalyst, a representative structural model (shown in Figure 3) with dimensions equivalent to the average particle size after reaction was used. These models allowed an approximate number of surface tungsten atoms to be counted and used as the number of available sites for reaction. As depicted in Figure 3a-f, the density of surface tungsten atoms on each facet differs greatly for each phase. α-WC possess a more uniform distribution and spacing of tungsten atoms, while the uneven surface and diverse number of facets yields a wider range of spacing between surface tungsten atoms with numerous terrace sites and clusters created by the intersection of cleaved planes. A thin shell encompassing both models was used to count the total number of surface tungsten atoms, and provides an overestimate of the number of active sites on the nanoparticle as all tungsten atoms on the surface of the nanoparticle morphology may not be accessible by reactant molecules. Further discussion of the determination of active sites and calculation of the turnover number is detailed in the Supporting Information.

WO_x-NR and WO_x-NP were carburized and characterized with XRD without reaction to determine the phase and structure of fresh carbide. As seen in Figure 1, W_xC-NR exhibits strong reflections at 31.5, 35.6, and 48.2° 2θ consistent with the (001), (100), and (101) facets, respectively, of the hexagonal α-WC phase. These reflections are absent from the W_xC-NP sample; instead a small reflection is present at 39.6° 2θ consistent with the (101) facet of the hexagonal β-W_2C phase. Preparation of visual models of each morphology in the observed crystal phase allows for further analysis of the exposed facets. As seen in Figure 3a, the nanorod morphology in the α-WC phase only exhibits two unique facets, (001) on the top and bottom basal planes and (100) on each of the four sides of the rod, while the nanoparticle morphology in the β-W_2C phase possesses multiple exposed facets and numerous step sites with uncoordinated tungsten atoms. Synthesized particles in either morphology could possess a number of inherent defects; however, the nanorods will exhibit a significantly lower ratio of defects, i.e. uncoordinated atoms, in comparison to the nanoparticles.

3.2 Dry methane reforming reactions

Fresh supported oxide nanomaterial samples were pelletized and carburized in situ before testing as catalysts for DMR. Atmospheric pressures have been noted to lessen the formation of coke on carbide catalysts,[45] and, therefore, were employed for testing of the various tungsten carbide morphologies to elucidate differences in coke resistance for each sample in addition to activity differences. A high temperature, 1173 K, was chosen for the reaction temperature, as it is consistent with the carburization temperature of tungsten carbide,[24, 42] and allows near complete conversion at atmospheric pressure.[5] Figure 4 shows the reaction data for each catalyst in terms of reactant conversion and product yield plotted against TON calculated from an approximate site density as detailed in the SI. It is evident that W_xC-NR undergoes an induction period for 3000 turnovers after which a pseudo-steady state is reached for 5000 turnovers, with 55% conversion of CO_2 and 45% conversion of CH_4. A 90% selectivity to CO suggests some oxidation may be occurring during the dissociation of CO_2 on the carbide surface, but this could also be associated with the reverse water-gas shift (RWGS) reaction occurring in parallel to the reforming pathway as has been noted in literature studies of carbides and other catalysts.[7] A low H_2 selectivity value of 66% supports the hypothesis of a prevalent RWGS pathway leading to the formation of water along with elevated CO_2 conversion. It is well noted in dry reforming literature that a H_2/CO ratio of less than unity points to the prevalence of a competing RWGS pathway, as the high temperature of the reaction in combination with high flow rates facilitates the reaction of hydrogen species formed from the dissociation of methane with abundant CO_2 to form CO and water.[53] After 8000 turnovers, the catalyst began to deactivate in a linear fashion, suggesting either surface oxidation or, more likely, surface coke formation was responsible for catalytic decay (which is in accordance with previous studies of deactivation on supported carbide catalysts).[11]

A similar wt.% loading of W_xC-NP reacted under the same conditions undergoes a comparable induction period

for 3000 turnovers, and then approaches the thermodynamic limit of conversion, ~98% for CH_4 and ~96% for CO_2, with conversions of 92% and 82% for CH_4 and CO_2, respectively, maintaining a pseudo-steady state for nearly one hundred thousand turnovers. A slight decrease in CH_4 conversion is observed after 35000 turnovers, with a corresponding decrease in H_2 yield. A similar analysis of selectivity for W_xC-NP reveals the likely presence of the RWGS reaction as the selectivity to H_2 lies near 50%. This observation suggests the nanoparticle morphology may promote the competing RWGS reaction; however, the prevalence of the RWGS reaction may be due to the presence of additional amounts of hydrogen on the catalyst surface at high conversions.

While both samples were loaded with nominally the same wt.% tungsten they display markedly different conversion under similar reaction conditions. Two associated hypotheses arise from this observation. W_xC-NP possesses a higher theoretical particle surface area in comparison with W_xC-NR which could lead to a higher number of exposed active sites for the nanoparticle morphology. In addition, although both phases have similar crystallographic symmetry, α-WC possess a low number of carbon vacancies, leading to a lower prevalence of unsaturated tungsten surface atoms, as discussed by Kurlov and Gusev,[54] on the W_xC-NR sample. In contrast, β-W_2C is inherently disordered with numerous carbon vacancies in a random distribution throughout the lattice likely leading to a high degree of unsaturated tungsten surface atoms.

XRD patterns for spent catalyst samples of W_xC-NR and W_xC-NP, denoted –sp, are shown in Figure 1. In the case of W_xC-NR-sp, it can be seen that there is a large amorphous region at 26° indicative of the presence of surface carbon, as well as a sharp reflection indicative of graphitic carbon formation, a feature that is also observed to a lesser extent for W_xC-NP. The carbide phase of W_xC-NR and W_xC-NP is undisturbed and no WO_3 reflections are observed in either spent sample, suggesting the deactivation mechanism is not through bulk oxidation However, the presence of surface oxides may still play an important role in the loss of activity for the nanorod sample. To further investigate the morphology of each catalyst, TEM was performed for each sample after reaction. HRTEM micrographs for W_xC-NR-sp in Figure 2c show growth parallel to the (001) plane of the tungsten carbide nanorods, with the (101) and (100) planes also clearly visible. Furthermore, a 2 nm thick layer of carbon is observed for the W_xC-NR sample in contrast with W_xC-NP, where few coke deposits are observed, as seen in Figure S2. This observation suggests that the rate of coke deposition is much slower for the nanoparticle sample than for the nanorod morphology. In order to determine the amount of carbon deposited during reaction, thermogravimetric analysis in air was performed on each spent catalyst after reaction. As seen in Figure S3, the amount of weight loss for the W_xC-NP-sp is quite similar to that of the bare support, and far less (20 wt% vs 33 wt%) than the spent W_xC-NR catalyst. A hypothesis to explain this difference is the presence of numerous edge sites along the (100) direction of the nanorod that promote carbon formation and are less active for the DMR reaction. In contrast, the nanoparticle is primarily composed of exposed (110), (002), and (-1-11) facets, which could explain the large disparity in activity between the two catalysts.

4. CONCLUSIONS

In conclusion, we have investigated the effect of phase and morphology on the activity and stability of tungsten carbide nanomaterials for methane DMR. We hypothesize the inherent disorder and presence of carbon vacancies in the β-W_2C phase nanoparticles leads to less coke deposition and higher conversion with a similar mass loading than the α-WC phase nanorods that do not possess the same degree of defects. These inherent carbon vacancies in the carbide lattice likely facilitate the oxidation/recarburization reaction that leads to higher activity while preserving the active catalyst and minimizing coke deposition. The correlation of activity and coke resistance with the inherent defects of the β-W_2C yields a potential avenue for increasing performance of carbide catalysts for dry methane reforming through defect engineering.

ASSOCIATED CONTENT

Supporting Information

Experimental procedures, particle size distributions, TEM images, and a detailed calculation of TON are available in the ESI.

ACKNOWLEDGMENTS

The authors thank Michael L. Stone for valuable discussions. This research was supported through a Research Agreement with Saudi Aramco, a Founding Member of the MIT Energy Initiative.

REFERENCES

(1) Lavoie, J.-M., Review on dry reforming of methane, a potentially more environmentally-friendly approach to the increasing natural gas exploitation. *Front. Chem.* **2014,** *2*, 81.
(2) Mikkelsen, M.; Jørgensen, M.; Krebs, F. C., The teraton challenge. A review of fixation and transformation of carbon dioxide. *Energy Environ. Sci.* **2010,** *3*, 43-81.

(3) Fujimoto, K.; Omata, K.; Nozaki, T.; Yamazaki, O.; Han, Y., Selective synthesis of liquid hydrocarbons from carbon dioxide and methane. *Energy Convers. Manage.* **1992,** *33*, 529-536.
(4) Wang, S.; Lu, G. Q.; Millar, G. J., Carbon Dioxide Reforming of Methane To Produce Synthesis Gas over Metal-Supported Catalysts: State of the Art. *Energy Fuels* **1996,** *10*, 896-904.
(5) Simakov, D. S. A.; Wright, M. M.; Ahmed, S.; Mokheimer, E. M. A.; Román-Leshkov, Y., Solar thermal catalytic reforming of natural gas: a review on chemistry, catalysis and system design. *Cat. Sci. Tech.* **2015,** *5*, 1991-2016.
(6) Guczi, L.; Stefler, G.; Geszti, O.; Sajó, I.; Pászti, Z.; Tompos, A.; Schay, Z., Methane dry reforming with CO2: A study on surface carbon species. *Appl. Catal., A* **2010,** *375*, 236-246.
(7) Arora, S.; Prasad, R., An overview on dry reforming of methane: strategies to reduce carbonaceous deactivation of catalysts. *RSC Adv.* **2016,** *6*, 108668-108688.
(8) Yao, Z.; Jiang, J.; Zhao, Y.; Luan, F.; Zhu, J.; Shi, Y.; Gao, H.; Wang, H., Insights into the deactivation mechanism of metal carbide catalysts for dry reforming of methane via comparison of nickel-modified molybdenum and tungsten carbides. *RSC Adv.* **2016,** *6*, 19944-19951.
(9) Pakhare, D.; Spivey, J., A review of dry (CO2) reforming of methane over noble metal catalysts. *Chem. Soc. Rev.* **2014,** *43*, 7813-7837.
(10) Iyer, M. V.; Norcio, L. P.; Kugler, E. L.; Dadyburjor, D. B., Kinetic Modeling for Methane Reforming with Carbon Dioxide over a Mixed-Metal Carbide Catalyst. *Ind. Eng. Chem. Res.* **2003,** *42*, 2712-2721.
(11) Brungs, A. J.; York, A. P. E.; Green, M. L. H., Comparison of the group V and VI transition metal carbides for methane dry reforming and thermodynamic prediction of their relative stabilities. *Catal. Lett.* **1999,** *57*, 65-69.
(12) Shao, H. F.; Kugler, E. L.; Ma, W. P.; Dadyburjor, D. B., Effect of temperature on structure and performance of in-house cobalt-tungsten carbide catalyst for dry reforming of methane. *Ind. Eng. Chem. Res.* **2005,** *44*, 4914-4921.
(13) Kislov, V. R.; Skudin, V. V.; Adamu, A., New bimetallic Mo2C–WC/Al2O3 membrane catalysts in the dry reforming of methane. *Kinet. Catal.* **2017,** *58*, 73-80.
(14) Oyama, S. T., Introduction to the chemistry of transition metal carbides and nitrides. In *The Chemistry of Transition Metal Carbides and Nitrides*, Oyama, S. T., Ed. Springer Netherlands: Dordrecht, 1996; pp 1-27.
(15) Ted Oyama, S., Crystal structure and chemical reactivity of transition metal carbides and nitrides. *J. Solid State Chem.* **1992,** *96*, 442-445.
(16) Oyama, S. T., Preparation and catalytic properties of transition metal carbides and nitrides. *Catal. Today* **1992,** *15*, 179-200.
(17) Ribeiro, F. H.; Dalla Betta, R. A.; Guskey, G. J.; Boudart, M., Preparation and surface composition of tungsten carbide powders with high specific surface area. *Chem. Mater.* **1991,** *3*, 805-812.
(18) Kunkel, C.; Vines, F.; Illas, F., Transition metal carbides as novel materials for CO2 capture, storage, and activation. *Energy Environ. Sci.* **2016,** *9*, 141-144.
(19) Michalsky, R.; Zhang, Y.-J.; Peterson, A. A., Trends in the Hydrogen Evolution Activity of Metal Carbide Catalysts. *ACS Catal.* **2014,** *4*, 1274-1278.
(20) Anasori, B.; Lukatskaya, M. R.; Gogotsi, Y., 2D metal carbides and nitrides (MXenes) for energy storage. *Nat. Rev. Mats.* **2017,** *2*, 16098.
(21) Alexander, A.-M.; Hargreaves, J. S. J., Alternative catalytic materials: carbides, nitrides, phosphides and amorphous boron alloys. *Chem. Soc. Rev.* **2010,** *39*, 4388-4401.
(22) Zou, X.; Zhang, Y., Noble metal-free hydrogen evolution catalysts for water splitting. *Chem. Soc. Rev.* **2015,** *44*, 5148-5180.
(23) Murugappan, K.; Anderson, E. M.; Teschner, D.; Jones, T. E.; Skorupska, K.; Román-Leshkov, Y., Operando NAP-XPS unveils differences in MoO3 and Mo2C during hydrodeoxygenation. *Nat. Catal.* **2018,** *1*, 960-967.
(24) Volpe, L.; Boudart, M., Compounds of molybdenum and tungsten with high specific surface area II: carbides. *J. Solid State Chem.* **1985,** *59*, 348-356.
(25) Ribeiro, F. H.; Dalla Betta, R. A.; Boudart, M.; Baumgartner, J.; Iglesia, E., Reactions of neopentane, methylcyclohexane, and 3,3-dimethylpentane on tungsten carbides: The effect of surface oxygen on reaction pathways. *J. Catal.* **1991,** *130*, 86-105.
(26) Iglesia, E.; Baumgartner, J. E.; Ribeiro, F. H.; Boudart, M., Bifunctional reactions of alkanes on tungsten carbides modified by chemisorbed oxygen. *J. Catal.* **1991,** *131*, 523-544.
(27) Levy, R. B.; Boudart, M., Platinum-Like Behavior of Tungsten Carbide in Surface Catalysis. *Science* **1973,** *181*, 547-549.

(28) Hunt, S. T.; Milina, M.; Wang, Z.; Roman-Leshkov, Y., Activating earth-abundant electrocatalysts for efficient, low-cost hydrogen evolution/oxidation: sub-monolayer platinum coatings on titanium tungsten carbide nanoparticles. *Energy Environ. Sci.* **2016,** *9*, 3290-3301.
(29) Hunt, S. T.; Milina, M.; Alba-Rubio, A. C.; Hendon, C. H.; Dumesic, J. A.; Román-Leshkov, Y., Self-assembly of noble metal monolayers on transition metal carbide nanoparticle catalysts. *Science* **2016,** *352*, 974-978.
(30) Vijayakumar, P.; Senthil Pandian, M.; Lim, S. P.; Pandikumar, A.; Huang, N. M.; Mukhopadhyay, S.; Ramasamy, P., Facile synthesis of tungsten carbide nanorods and its application as counter electrode in dye sensitized solar cells. *Mater. Sci. Semicond. Process.* **2015,** *39*, 292-299.
(31) Hunt, S. T.; Kokumai, T. M.; Zanchet, D.; Román-Leshkov, Y., Alloying Tungsten Carbide Nanoparticles with Tantalum: Impact on Electrochemical Oxidation Resistance and Hydrogen Evolution Activity. *J. Phys. Chem. C* **2015,** *119*, 13691-13699.
(32) Roy, C.; Rao, R. R.; Stoerzinger, K. A.; Hwang, J.; Rossmeisl, J.; Chorkendorff, I.; Shao-Horn, Y.; Stephens, I. E. L., Trends in Activity and Dissolution on RuO2 under Oxygen Evolution Conditions: Particles versus Well-Defined Extended Surfaces. *ACS Energy Lett.* **2018,** *3*, 2045-2051.
(33) Peng, C.; Yang, X.; Li, Y.; Yu, H.; Wang, H.; Peng, F., Hybrids of Two-Dimensional Ti3C2 and TiO2 Exposing {001} Facets toward Enhanced Photocatalytic Activity. *ACS Appl. Mater. Interfaces* **2016,** *8*, 6051-6060.
(34) Madey, T. E.; Guan, J.; Nien, C. H.; Dong, C. Z.; Tao, H. S.; Campbell, R. A., Faceting Induced By Ultrathin Metal Films On W(111) And Mo(111): Structure, Reactivity, And Electronic Properties. *Surf. Rev. Lett.* **1996,** *03*, 1315-1328.
(35) Chiu, C.-Y.; Chung, P.-J.; Lao, K.-U.; Liao, C.-W.; Huang, M. H., Facet-Dependent Catalytic Activity of Gold Nanocubes, Octahedra, and Rhombic Dodecahedra toward 4-Nitroaniline Reduction. *J. Phys. Chem. C* **2012,** *116*, 23757-23763.
(36) Michalsky, R.; Zhang, Y.-J.; Medford, A. J.; Peterson, A. A., Departures from the Adsorption Energy Scaling Relations for Metal Carbide Catalysts. *J. Phys. Chem. C* **2014,** *118*, 13026-13034.
(37) Brungs, A. J.; York, A. P. E.; Claridge, J. B.; Márquez-Alvarez, C.; Green, M. L. H., Dry reforming of methane to synthesis gas over supported molybdenum carbide catalysts. *Catal. Lett.* **2000,** *70*, 117-122.
(38) P. E. York, A.; B. Claridge, J.; J. Brungs, A.; Chi Tsang, S.; L. H. Green, M., Molybdenum and tungsten carbides as catalysts for the conversion of methane to synthesis gas using stoichiometric feedstocks. *Chem. Commun.* **1997**, 39-40.
(39) Iyer, M. V.; Norcio, L. P.; Punnoose, A.; Kugler, E. L.; Seehra, M. S.; Dadyburjor, D. B., Catalysis for Synthesis Gas Formation from Reforming of Methane. *Top. Catal.* **2004,** *29*, 197-200.
(40) Shi, C.; Zhang, A.; Li, X.; Zhang, S.; Zhu, A.; Ma, Y.; Au, C., Ni-modified Mo2C catalysts for methane dry reforming. *Appl. Catal., A* **2012,** *431-432*, 164-170.
(41) Claridge, J. B.; York, A. P. E.; Brungs, A. J.; Marquez-Alvarez, C.; Sloan, J.; Tsang, S. C.; Green, M. L. H., New Catalysts for the Conversion of Methane to Synthesis Gas: Molybdenum and Tungsten Carbide. *J. Catal.* **1998,** *180*, 85-100.
(42) Hunt, S. T.; Nimmanwudipong, T.; Román-Leshkov, Y., Engineering Non-sintered, Metal-Terminated Tungsten Carbide Nanoparticles for Catalysis. *Angew. Chem., Int. Ed. Engl.* **2014,** *53*, 5131-5136.
(43) Hendon, C. H.; Hunt, S. T.; Milina, M.; Butler, K. T.; Walsh, A.; Román-Leshkov, Y., Realistic Surface Descriptions of Heterometallic Interfaces: The Case of TiWC Coated in Noble Metals. *J. Phys. Chem. Lett.* **2016,** *7*, 4475-4482.
(44) Neylon, M. K.; Choi, S.; Kwon, H.; Curry, K. E.; Thompson, L. T., Catalytic properties of early transition metal nitrides and carbides: n-butane hydrogenolysis, dehydrogenation and isomerization. *Appl. Catal., A* **1999,** *183*, 253-263.
(45) Yan, Q.; Lu, Y.; To, F.; Li, Y.; Yu, F., Synthesis of tungsten carbide nanoparticles in biochar matrix as a catalyst for dry reforming of methane to syngas. *Cat. Sci. Tech.* **2015,** *5*, 3270-3280.
(46) Shao, H.; Kugler, E. L.; Ma, W.; Dadyburjor, D. B., Effect of Temperature on Structure and Performance of In-House Cobalt−Tungsten Carbide Catalyst for Dry Reforming of Methane. *Ind. Eng. Chem. Res.* **2005,** *44*, 4914-4921.
(47) Lee, K.; Seo, W. S.; Park, J. T., Synthesis and Optical Properties of Colloidal Tungsten Oxide Nanorods. *J. Am. Chem. Soc.* **2003,** *125*, 3408-3409.
(48) Soultanidis, N.; Zhou, W.; Kiely, C. J.; Wong, M. S., Solvothermal Synthesis of Ultrasmall

Tungsten Oxide Nanoparticles. *Langmuir* **2012,** *28*, 17771-17777.
(49) Efstathiou, A. M.; Kladi, A.; Tsipouriari, V. A.; Verykios, X. E., Reforming of Methane with Carbon Dioxide to Synthesis Gas over Supported Rhodium Catalysts: II. A Steady-State Tracing Analysis: Mechanistic Aspects of the Carbon and Oxygen Reaction Pathways to Form CO. *J. Catal.* **1996,** *158*, 64-75.
(50) Sarusi, I.; Fodor, K.; Baán, K.; Oszkó, A.; Pótári, G.; Erdőhelyi, A., CO2 reforming of CH4 on doped Rh/Al2O3 catalysts. *Catal. Today* **2011,** *171*, 132-139.
(51) Zhang, Z. L.; Tsipouriari, V. A.; Efstathiou, A. M.; Verykios, X. E., Reforming of Methane with Carbon Dioxide to Synthesis Gas over Supported Rhodium Catalysts: I. Effects of Support and Metal Crystallite Size on Reaction Activity and Deactivation Characteristics. *J. Catal.* **1996,** *158*, 51-63.
(52) Brunauer, S.; Emmett, P. H.; Teller, E., Adsorption of Gases in Multimolecular Layers. *J. Am. Chem. Soc.* **1938,** *60*, 309-319.
(53) Serrano-Lotina, A.; Daza, L., Influence of the operating parameters over dry reforming of methane to syngas. *Int. J. Hydrogen Energy* **2014,** *39*, 4089-4094.
(54) Kurlov, A. S.; Gusev, A. I., Tungsten carbides and W-C phase diagram. *Inorg. Mater.* **2006,** *42*, 121-127.

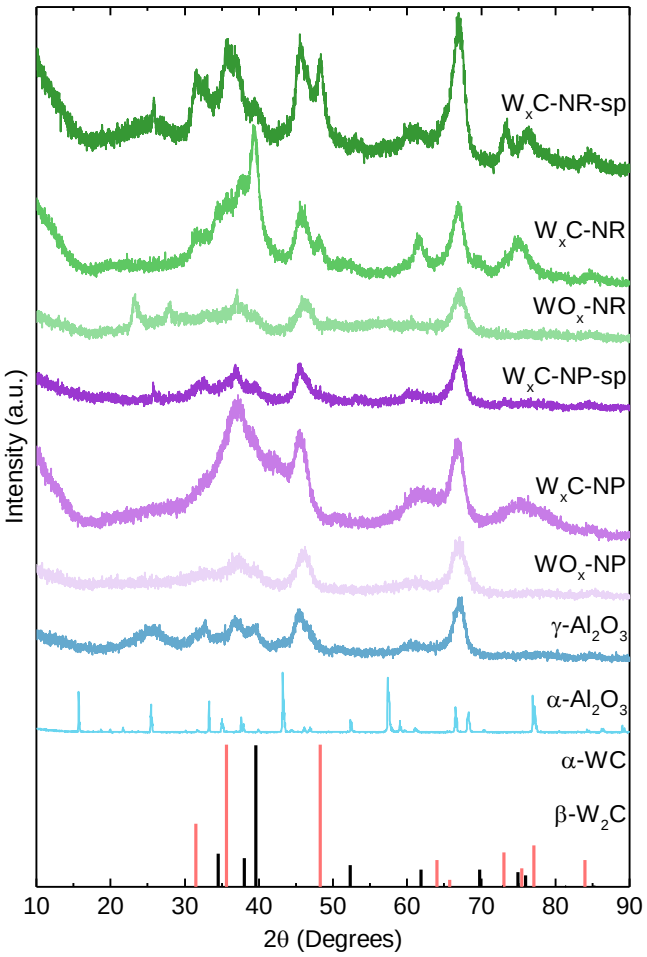

Figure 1. PXRD patterns of spent (denoted W_xC-NR/NP–sp), carburized (denoted W_xC-NR/NP), fresh supported (denoted WO_x-NR/NP) catalysts, γ-Al_2O_3, α-Al_2O_3, and reference patterns of α-WC, and β-W_2C.

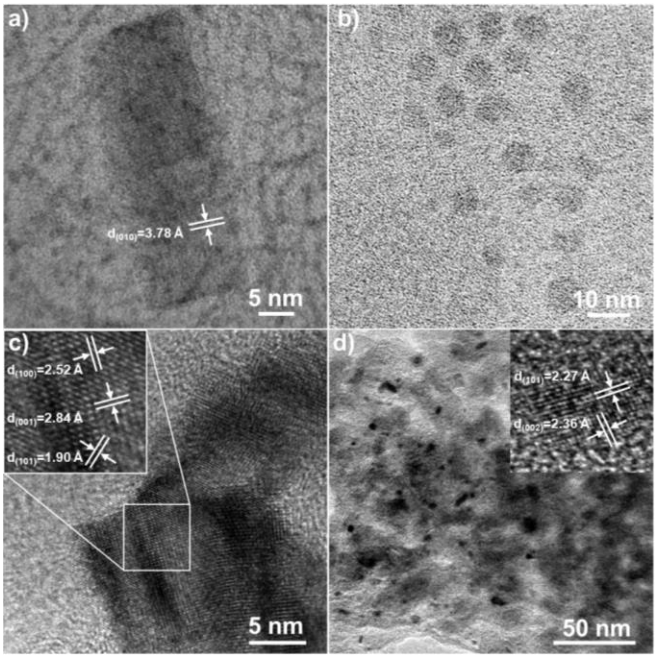

Figure 2. TEM images of fresh supported (a) WO_x-NR, (b) WO_x-NP, and spent (c) W_xC-NR-sp, (d) W_xC-NP-sp catalysts.

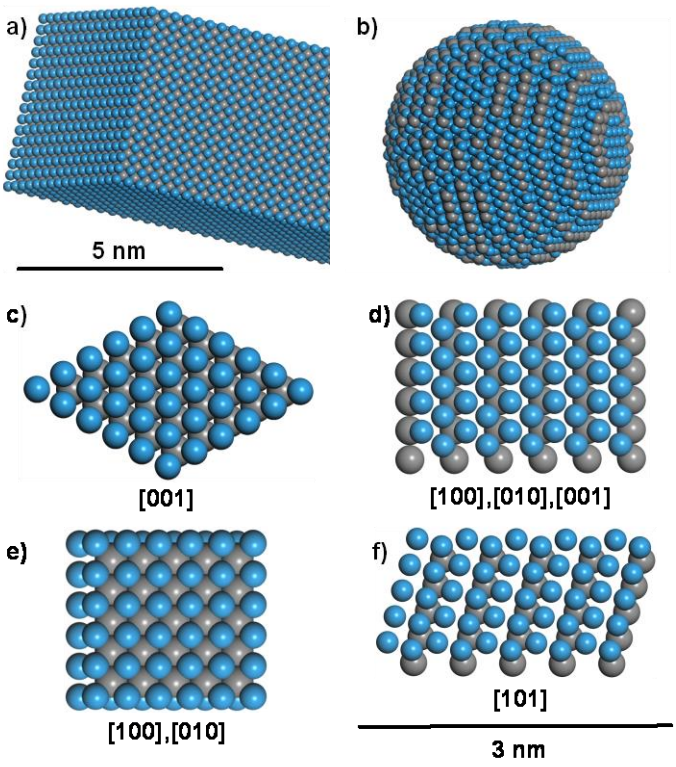

Figure 3. (a) α-WC nanorod (W_xC-NR) and (b) β-W_2C nanoparticle (W_xC-NP) structures. (c,e) Top view of α-WC facets, (d,f) top view of β-W_2C facets.

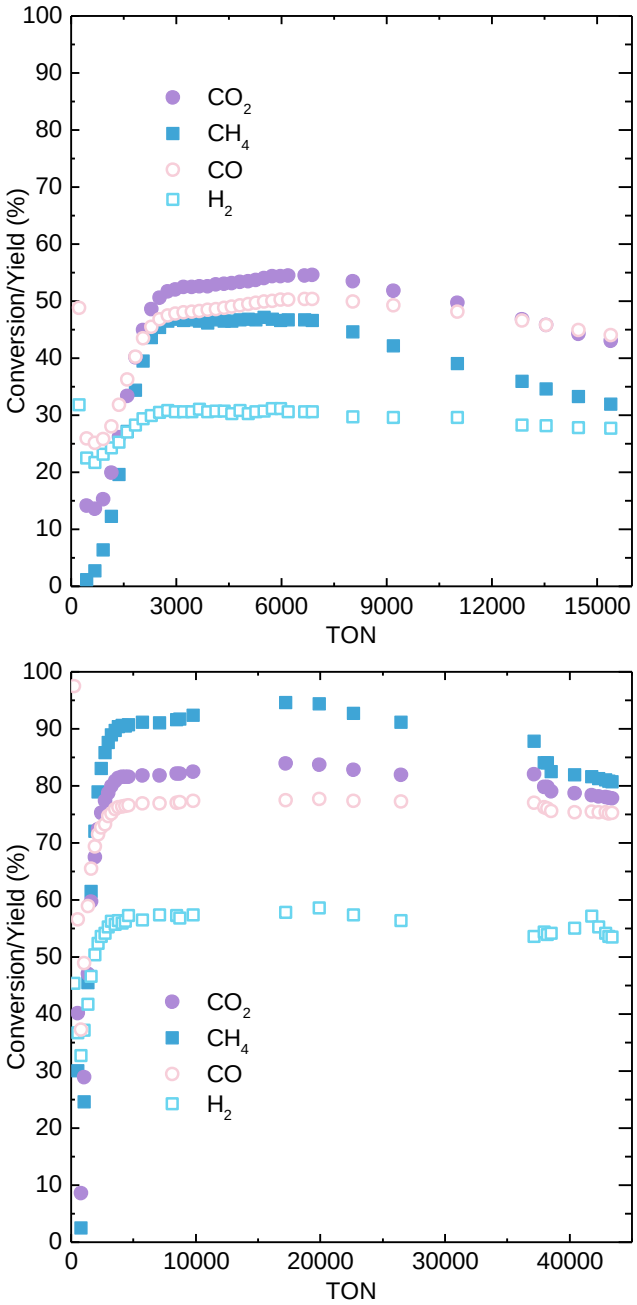

Figure 4: Reaction data for DMR reactions performed with W_xC-NR (top) and W_xC-NP (bottom) supported on γ-Al_2O_3. (200 mg catalyst, 10 wt.% W, 1173 K, 1 atm, CH_4/CO_2 = 1, 30 mL min^{-1})